nature catalysis

ARTICLES

https://doi.org/10.1038/s41929-020-00525-6

Check for updates

# High-valence metals improve oxygen evolution reaction performance by modulating 3*d* metal oxidation cycle energetics

Bo Zhang[1,12]✉, Lie Wang[1,12], Zhen Cao[2,12], Sergey M. Kozlov[2], F. Pelayo García de Arquer[3], Cao Thang Dinh[3], Jun Li[4], Ziyun Wang[3], Xueli Zheng[3], Longsheng Zhang[1], Yunzhou Wen[1], Oleksandr Voznyy[3], Riccardo Comin[3], Phil De Luna[3], Tom Regier[5], Wenli Bi[6], E. Ercan Alp[7], Chih-Wen Pao[8], Lirong Zheng[9], Yongfeng Hu[5], Yujin Ji[10], Youyong Li[10], Ye Zhang[11], Luigi Cavallo[2]✉, Huisheng Peng[1]✉ and Edward H. Sargent[3]✉

**Multimetal oxyhydroxides have recently been reported that outperform noble metal catalysts for oxygen evolution reaction (OER). In such 3*d*-metal-based catalysts, the oxidation cycle of 3*d* metals has been posited to act as the OER thermodynamic-limiting process; however, further tuning of its energetics is challenging due to similarities among the electronic structures of neighbouring 3*d* metal modulators. Here we report a strategy to reprogram the Fe, Co and Ni oxidation cycles by incorporating high-valence transition-metal modulators X (X = W, Mo, Nb, Ta, Re and MoW). We use in situ and ex situ soft and hard X-ray absorption spectroscopies to characterize the oxidation transition in modulated NiFeX and FeCoX oxyhydroxide catalysts, and conclude that the lower OER overpotential is facilitated by the readier oxidation transition of 3*d* metals enabled by high-valence modulators. We report an ~17-fold mass activity enhancement compared with that for the OER catalysts widely employed in industrial water-splitting electrolysers.**

The oxygen evolution reaction (OER), used at the anodic side in hydrogen evolution and carbon dioxide reduction systems, suffers from an excess voltage (overpotential) relative to that mandated by the thermodynamic value of the products[1–9]. Since the cost of renewable electricity will dominate the cost of renewable fuel production[10], lowering the overpotentials contributes to lowering the cost of producing synthetic fuels[11].

First-row (3*d*) transition-metal oxides are promising electrocatalysts for OER and are used in commercial electrolysers[6,9,12–15]. The catalytic performance of multimetal oxyhydroxides consisting of 3*d* transition metals is improved by introducing additional elements that affect the electronic structure of the catalyst as a whole[16–20], influencing the adsorption energies of intermediate species. This strategy was employed in ternary systems such as FeCoW metal oxyhydroxide to achieve catalysts that, with optimized OH*, O* and OOH* adsorption energies on the surface of the catalyst, exhibited OER performance superior to that of noble metal catalysts[16].

It has been noted that in single-metal β-CoOOH frameworks, Co oxidation cycling through a $Co^{3+}/Co^{4+}$ transition is the thermodynamic-limiting process (TLP), and the largest contributor to the OER overpotential[21]. Modelling has predicted that facet manipulation in this framework can lead to a shift in cycling in $Co^{3+}/Co^{4+}$ towards a lower valence of $Co^{2+}/Co^{3+}/Co^{4+}$, in turn enabling lower overpotentials[21]. This intriguing prediction has, however, not yet been proven in multinary 3*d* metal oxyhydroxide systems. Previous work has demonstrated the incorporation of high-valence W (ref. [22]), Ta (ref. [22]) and Mo (ref. [23]) to stabilize the otherwise unstable low-charge $Fe^{2+}$.

Here we posit a general doping strategy: the addition of metallic dopants with high-valence charges modulate 3*d* metals (Fe, Co and Ni) towards lower energetics of valence charge transition, and hence better catalytic OER performance. We present a physical model of OER in multinary metal oxyhydroxides, screen different dopants and study the modulation of Fe, Co and Ni valence states. We synthesize and characterize, using in situ and ex situ X-ray absorption spectroscopy (XAS), catalysts consisting of NiFeX and FeCoX (where X = W, Mo, Nb, Ta, Re and MoW), and find good agreement with modelling results. As a result, we report a 17-fold mass activity enhancement compared with the state-of-art catalysts in industrial hydrogen generation systems.

## Results

**Density functional theory (DFT) calculations.** We began by building a FeCo oxyhydroxide model based on an established

[1]State Key Laboratory of Molecular Engineering of Polymers, Department of Macromolecular Science and Laboratory of Advanced Materials, Fudan University, Shanghai, China. [2]KAUST Catalysis Center, King Abdullah University of Science and Technology (KAUST), Thuwal, Saudi Arabia. [3]Department of Electrical and Computer Engineering, University of Toronto, Toronto, Ontario, Canada. [4]Institute of Chemical Sciences and Engineering, École polytechnique fédérale de Lausanne, Lausanne, Switzerland. [5]Canadian Light Source, Inc. (CLSI), Saskatoon, Saskatchewan, Canada. [6]Department of Physics, University of Alabama at Birmingham, Birmingham, AL, USA. [7]Advanced Photon Source, Argonne National Laboratory, IL, USA. [8]National Synchrotron Radiation Research Center, Science-Based Industrial Park, Hsinchu, Taiwan. [9]Beijing Synchrotron Radiation Facility, Institute of High Energy Physics, Chinese Academy of Sciences, Beijing, China. [10]Institute of Functional Nano & Soft Materials (FUNSOM) and Jiangsu Key Laboratory for Carbon-Based Functional Materials & Devices, Soochow University, Suzhou, China. [11]College of Engineering and Applied Sciences, Nanjing University, Nanjing, China. [12]These authors contributed equally: Bo Zhang, Lie Wang, Zhen Cao. ✉e-mail: bozhang@fudan.edu.cn; luigi.cavallo@kaust.edu.sa; penghs@fudan.edu.cn; ted.sargent@utoronto.ca

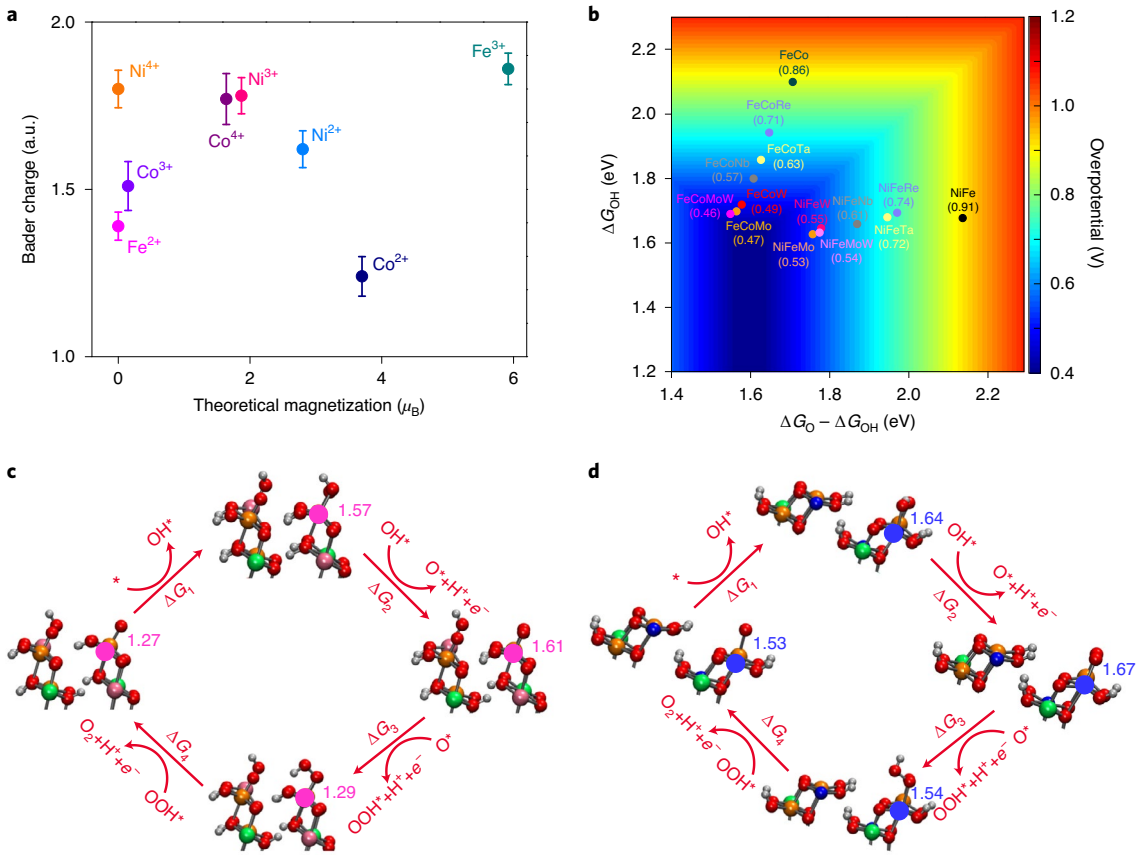


**Fig. 1 | Density functional simulation findings. a**, Statistical analysis of the calculated Bader charge and magnetization obtained for Fe, Co and Ni within the oxyhydroxide framework from ~200 different configurations. The computed relative magnetizations for each component are consistent with the values predicted from crystal field theory for an octahedral environment. The error bars were calculated as the standard deviation: s.d. $= \sqrt{\sum_{i=1}^{n}(x_i - \bar{x})^2/(n-1)}$. **b**, Two-dimensional map of the overpotentials generated by assuming $\Delta E_{OOH} = E_{OH} + 3.2$ (ref. [21]) for different dopants in FeCoX and NiFeX catalysts: the overpotential can be reduced significantly with the high-valence charge metals. **c**,**d**, The OER cycles for FeCoX (**c**) and NiFeX (**d**), with the terminal group determined by the Pourbaix calculations (pink, Co; orange, Fe; blue, Ni; green, high-valence metal; red, O; grey, H), and the Bader charge on the active metal site is listed. a.u., arbitrary units.

computational framework[21] (Fig. 1 and Supplementary Fig. 1). The surface terminal groups were determined per the Pourbaix diagram (region (i) in Supplementary Fig. 2), and the trend of electronic properties of the metal atoms within the FeCoOOH model was investigated via the Bader charge and magnetization (Fig. 1a). Computational studies revealed that Co before OER exhibits a ~3+ charge, leading to a 3+/4+ transition cycle during OER, corresponding to the TLP due to $OH^*$ formation on the catalyst surface, which agreed well with the literature[21].

In computational studies, we doped high-valence metals into FeCo oxyhydroxides, forming FeCoX systems (X = Mo, W, Nb, Ta and Re), and Co and Fe showed a lower charge state (see Fig. 1a, Supplementary Figs. 3 and 4 and Supplementary Table 1). The OER cycle of the FeCoX catalysts demonstrates a lower valence charge transition of the Co active site (Fig. 1c), in contrast with the conventional high-valence charge transition cycle. FeCoX systems were found to enable the lowest overpotentials for OER in this system (Fig. 1b and Supplementary Table 2). We ascribed this decrement in overpotential to the lower electron affinity of active sites in the FeCoX system compared to that of the FeCo control, which reduces the energy required to stimulate electron transfer.

We extended the model to NiFe oxyhydroxide systems using the same metal dopants (Supplementary Fig. 5), and the surface terminal groups were also determined per the Pourbaix diagram (region (i) in Supplementary Fig. 6). We found that all studied NiFeX oxyhydroxides with higher valence charge dopants induced lower oxidation states of Ni and Fe than those in the pristine NiFe oxyhydroxide controls (Fig. 1a, Supplementary Figs. 7 and 8 and Supplementary Table 1), leading to a lower charge oxidation cycling of active sites during OER and therefore decreased overpotential (Fig. 1b,d and Supplementary Table 3).

Based on the fact that X = Mo and W lead to the highest predicted activity, we further evaluated the overpotential of the quaternary metal oxyhydroxides, consisting of two best dopants together. It was found that the predicted activity can be further improved in FeCoX systems (FeCoMoW in Fig. 1b).

**Materials synthesis and characterization.** We sought to investigate experimentally these concepts, preparing a suite of NiFeX and FeCoX oxyhydroxides and controls. We used a room-temperature sol-gel process[16]; after drying in vacuum, samples in the powder form were obtained (Supplementary Fig. 9). High-resolution transmission electron microscopy (HRTEM), selected-area electron diffraction, energy-dispersive X-ray spectroscopy mapping and X-ray diffraction (XRD) (Supplementary Figs. 10–24) revealed an amorphous structure. TEM images (Supplementary Figs. 10–23) and laser particle size analysis (Supplementary Fig. 25) also show that these catalysts form agglomerated particles with sizes above 100 nm. We further performed extended X-ray absorption fine structure characterization to evaluate the distribution of different metals. Taking

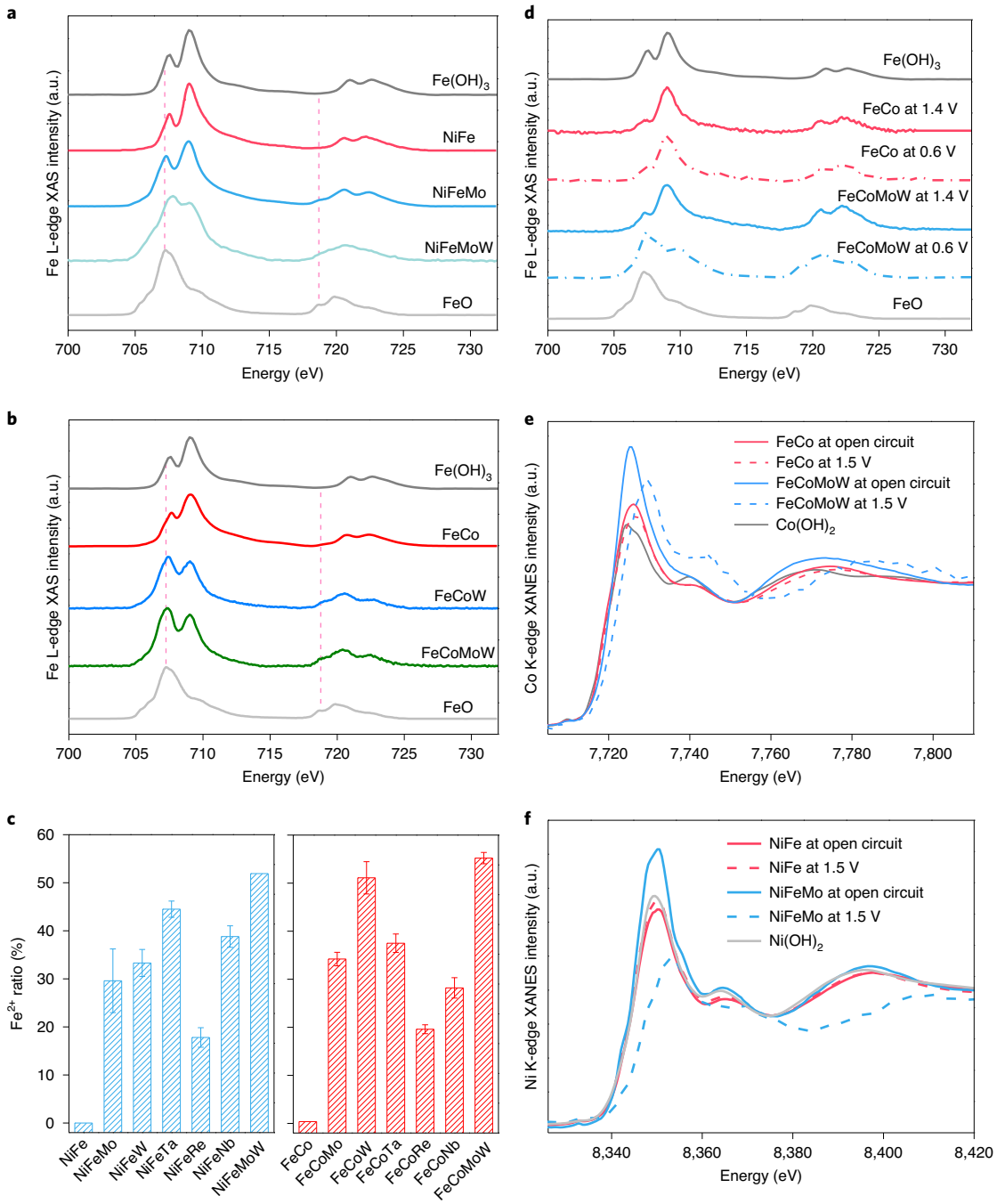


**Fig. 2 | Oxidation state transition of 3*d* metal in modulated catalysts. a**, TEY sXAS scans of NiFe, NiFeMo and NiFeMoW at the Fe L edge. **b**, TEY sXAS scans of FeCo, FeCoW, and FeCoMoW at the Fe L edge. **c**, Concentration of $Fe^{2+}$ species in all NiFeX and FeCoX samples. $Fe^{2+}$ data are obtained by linear combination analysis of Fe L-edge TEY sXAS results. **d**, The in situ Fe L-edge TEY sXAS spectra of FeCo and FeCoMoW. **e**, The in situ Co K-edge XANES spectra of FeCo and FeCoMoW. **f**, In situ Ni K-edge XANES spectra of NiFe and NiFeMo.

the FeCoMoW sample, for example (Supplementary Fig. 26), the Mo K-edge and W $L_3$-edge extended X-ray absorption fine structure and fitting results indicate that peaks associated with Mo-O-Co/Fe and W-O-Co/Fe are presented. These suggest that Mo, W and the 3*d* metal in the FeCoMoW sample were dispersed efficiently, which is in alignment with the structures we modelled, and is required to maximize the effect of modulation[16].

To characterize the oxidation state of 3*d* metal atoms in these materials before OER, we carried out ex situ soft XAS (sXAS) measurements monitoring 2*p* to 3*d* transitions in the L edges of 3*d* metals in total electron yield (TEY) mode, which is surface sensitive and valence sensitive[24,25]. NiFe and FeCo samples (Fig. 2a,b) yielded a significant amount of trivalent $Fe^{3+}$. In contrast, NiFeMo, NiFeMoW, FeCoMo and FeCoMoW exhibited a dominant amount of $Fe^{2+}$ species with the main peak at 707.2 eV and a shoulder peak at 718.7 eV at the $L_3$ edge (Fig. 2a,b). A series of time-dependent Fe L-edge XAS measurements was also performed to eliminate the possible beam damage from XAS to form the $Fe^{2+}$ (Supplementary Note 1 and Supplementary Fig. 27). Thereafter, linear combination fitting of these spectra over two reference Fe oxides (FeO for $Fe^{2+}$

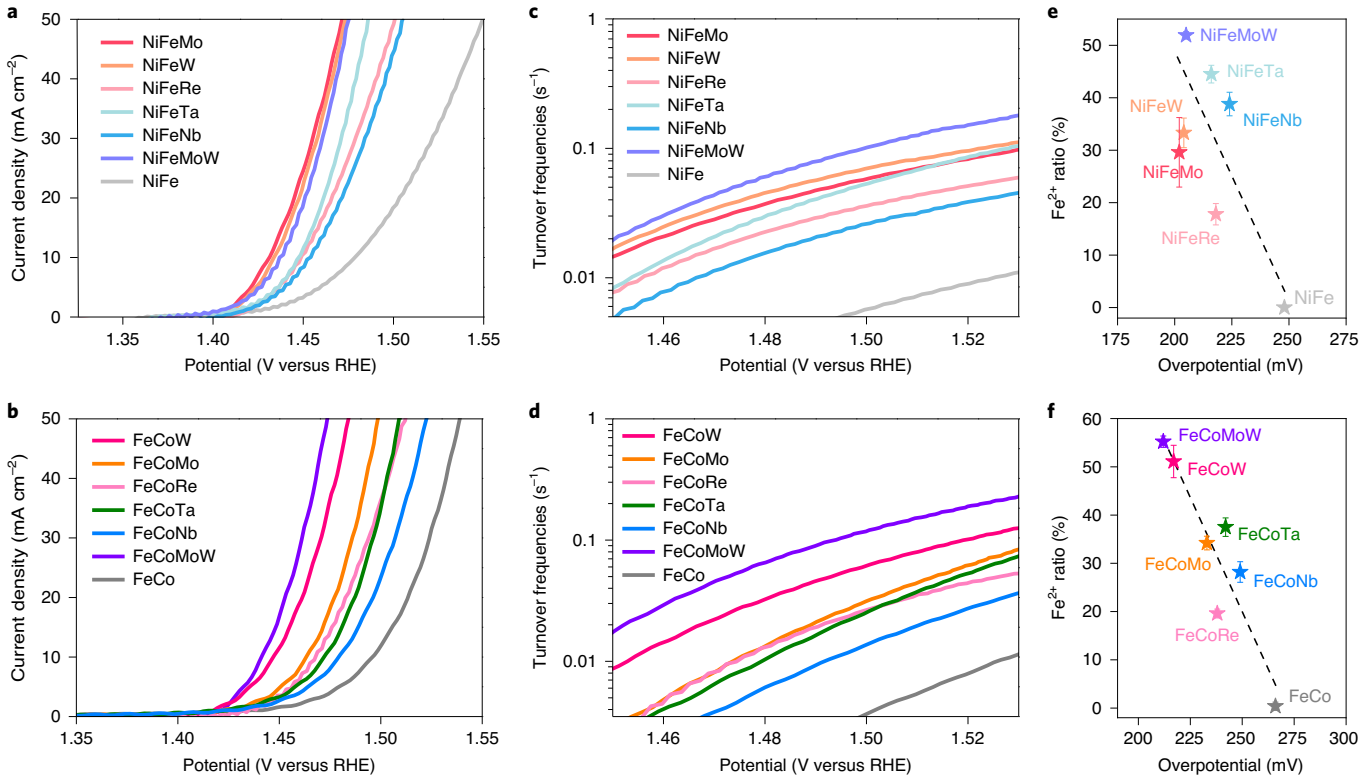


**Fig. 3 | Performance of NiFeX and FeCoX catalysts in 1 M KOH electrolyte at 25 °C. a**,**b**, OER polarization curves of NiFeX catalysts (**a**) and FeCoX catalysts (**b**) on carbon paper measured with a 5 mV $s^{-1}$ scan rate, with 95% *iR* correction. **c**,**d**, Turnover frequency trends as a function of potential for NiFeX catalysts (**c**) and FeCoX catalysts (**d**) on carbon paper measured with a 5 mV $s^{-1}$ scan rate, with 95% *iR* correction. **e**,**f**, Overpotentials at current density 10 mA $cm^{-2}$ tested versus $Fe^{2+}$ ratio in NiFeX catalysts (**e**) and FeCoX catalysts (**f**). RHE, reversible hydrogen electrode.

and $Fe(OH)_3$ for $Fe^{3+}$) allowed us to estimate the molar ratio of $Fe^{2+}$ and $Fe^{3+}$ (Supplementary Figs. 28 and 29), with the results shown in Fig. 2c and Supplementary Table 4. The high-valence metal modulated NiFe and FeCo samples exhibited higher $Fe^{2+}$ percentages than those binary controls, in agreement with DFT predictions on the trend of oxidation states.

Furthermore, we measured the oxidation state of Fe using off-line Mössbauer spectroscopy in transmission mode for FeCoMoW (Supplementary Fig. 30) and hard XAS in Fe K-edge for NiFeMo (Supplementary Fig. 31). Both Mössbauer spectra and K-edge X-ray absorption near edge structure (XANES) results showed significant $Fe^{2+}$. After linear combination fitting with reference samples (FeO for $Fe^{2+}$ and $Fe(OH)_3$ for $Fe^{3+}$), the results show a decreased ratio of $Fe^{2+}$ (11%) in FeCoMoW and $Fe^{2+}$ (20%) in NiFeMo compared to the Fe L-edge XAS results, which is a finding we ascribe to the fact that L-edge XAS is more surface sensitive than that of K-edge XAS and Mössbauer spectroscopy[25,26]. This suggests that the high-valence-metal modulation on 3*d* metals is more prominent on the catalyst surface, which can therefore tune the oxidation cycle energetics of 3*d* metals and the adsorption energies of intermediate species during the OER[16].

To assess the influence of high-valence metals on the oxidation transition of 3*d* metals, we carried out in situ Fe L-edge XAS under different applied potentials. First, we applied a bias of +1.4 V at the OER region to oxidize all Fe atoms to $Fe^{3+}$ in both FeCoMoW and FeCo samples (Fig. 2d). When the bias was changed to +0.6 V (0.1 V lower than the thermodynamic equilibrium potential of $Fe^{3+}/Fe^{2+}$), $Fe^{3+}$ in the FeCoMoW sample switched to a +2 oxidation state, while it did not change in the FeCo sample. This suggests that the oxidation transition of Fe occurs easier in FeCoMoW than it does in the binary control, which is consistent with DFT calculations.

We further conducted in situ Co K-edge (Fig. 2e) and L-edge XAS (Supplementary Fig. 32). At the initial state (before the OER) of all the studied FeCo-based samples, Co is in a $Co^{2+}$ configuration. At oxidizing bias during the OER, $Co^{2+}$ species were fully oxidized to higher valence states in the FeCoMoW sample, but they retained a $Co^{2+}$ character in FeCo. Upon switching the applied potential from 1.5 to 1.2 V (Supplementary Fig. 33), the oxidation state of Co changed to a low valence in the FeCoMoW sample, which did not happen in the FeCo sample. The ex situ Co L-edge XAS spectra after the OER (Supplementary Fig. 34) also showed consistent results. Furthermore, the oxidation transition of Ni in NiFe during the OER was also studied by in situ Ni K-edge XAS (Fig. 2f), and a similar conclusion was obtained.

The above XAS results indicate that the energy barriers of the oxidation transition of 3*d* metals are lower in high-valence-metal modulated systems than in binary controls. Previous studies have shown that 3*d* metal oxides with a lower oxidation barrier exhibit increased OER activities[27–29]. The present DFT studies also predicted that more facile oxidation transitions of 3*d* metals lead to increased OER activity. We further characterized the oxidation of high-valence metal during OER: the results indicate that the oxidation state did not change (Supplementary Note and Supplementary Fig. 35).

**Electrocatalytic performance.** We sought then to characterize the catalytic performance of the series of NiFeX and FeCoX oxyhydroxides in the three-electrode configuration in 1 M KOH electrolytes at room temperature (see Methods). As shown in Fig. 3, NiFeX and FeCoX exhibit lower overpotentials at 10 mA $cm^2$, an improvement of 37 mV and 54 mV compared with those of NiFe and FeCo catalysts, respectively (Supplementary Table 4). When

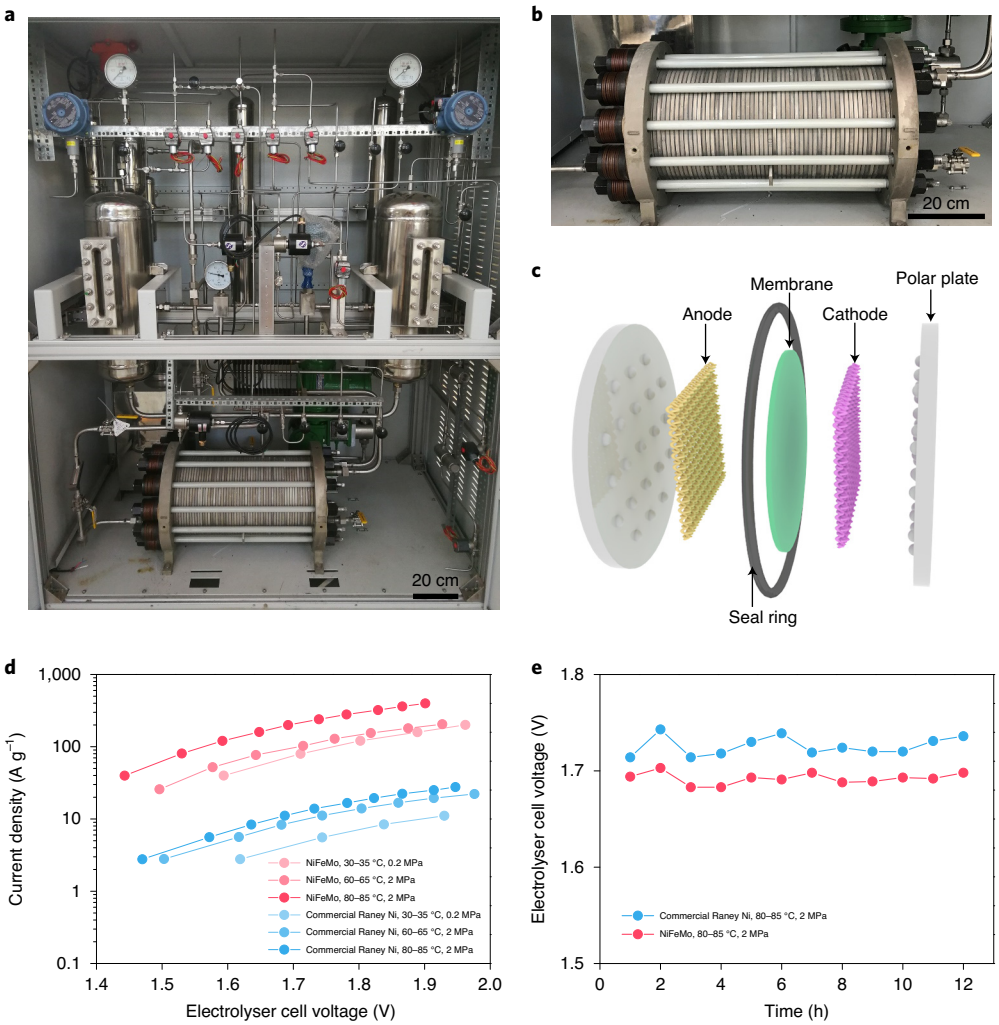


**Fig. 4 | Performance of NiFeMo catalysts in industrial electrolyser systems. a**, Photograph of an industrial electrolyser device. **b**, Enlarged view of the industrial electrolyser. **c**, Schematic illustration of the structure of an electrolyser cell. **d**, Polarization curves measured during water electrolysis using a NiFeMo electrode (red) and a commercial Raney Ni electrode (blue) as an anode, respectively, and a commercial Ru electrode as a cathode. **e**, The cell voltage of the electrolyser held at 300 mA cm$^{-2}$ for 12 h at 80–85 °C and 2 MPa.

compared with previous reports under the same testing conditions[30], the overpotential of NiFeMo is only 180 mV at 10 mA cm$^2$ (Supplementary Fig. 36).

To challenge further the posited link between $Fe^{2+}$ and the catalytic performance for OER, we varied the composition and checked the relative concentrations of $Fe^{2+}$ in each sample obtained using Fe L-edge XAS in TEY mode. For NiFe-based catalysts, the NiFeMo, NiFeW, NiFeNb, NiFeTa, NiFeRe and NiFeMoW exhibited significantly higher $Fe^{2+}$ ratio than that of the NiFe control, in agreement with the simulation results (Figs. 1 and 3e). For FeCo-based catalysts, a higher ratio of $Fe^{2+}$ led to lower overpotentials (Figs. 1 and 3f). Note that, although the catalysts with a higher $Fe^{2+}$ content result in lower overpotentials, the correlation is not perfect and there are some exceptions. In addition, a possible correlation between the dopants' covalent radii and performance was also investigated, and no clear correlation was found (Supplementary Fig. 37).

To distinguish the effects of catalyst surface area versus intrinsic performance, we investigated the turnover frequencies (TOFs). We used data obtained in 1 M KOH electrolyte at room temperature with 95% *iR* correction (where *i* is current measured and *R* is resistance) at different potentials to calculate TOFs. NiFeMoW and FeCoMoW outperform control samples, exhibiting approximately 17 times and 21 times higher TOFs than binary NiFe and FeCo controls at 300 mV overpotential, respectively (Fig. 3c,d).

**Performance under industrial conditions.** We also carried out the same testing under industrial conditions (30% KOH and at 85 °C), and observed trends that are consistent with those reported above (Supplementary Fig. 38). The corresponding mass activities of the NiFeX and FeCoX based on the total loading mass of the ternary and quaternary oxides are enhanced compared with the NiFe and FeCo controls (Supplementary Fig. 39). To characterize performance stability, we carried out water electrolysis by using NiFeMo catalysts and a commercial Ru electrode as anode and cathode, respectively. The resultant electrolyser delivered 300 mA cm$^{-2}$ at ~1.7 V consistently over 120 h (Supplementary Fig. 40), indicating high stability of the catalysts. We also carried out water oxidation by cyclic voltammetry measurements at 50 mV s$^{-1}$, and observed no appreciable decrease in the current densities over 2,000 cycles (Supplementary Fig. 41). To assess the performance of the catalysts on an industrial scale, we implemented these in industrial hydrogen generation systems (Fig. 4a). The central part of the system is the electrolyser (Fig. 4b,c). Under various applied cell potentials, the current densities (normalized by loading mass) of the cell

with the NiFeMo electrode are 17 times higher than the cell with a commercial Raney Ni electrode (Fig. 4d). When compared at identical current density, NiFeMo also exhibits a lower cell voltage compared with Raney Ni catalysts. We observed no appreciable increase in the cell voltage during initial studies of 12-h continuous operation (Fig. 4e).

## Conclusions

In summary, this work describes how the incorporation of high-valence metal modulators promotes the catalytic activity of multinary 3*d* metal compounds for OER. We offer a picture wherein the modulators lower the oxidation states of surface active sites (for example, Fe, Co and Ni) within their respective oxidation cycles. A synthetic route that seeks the homogeneous addition of such dopants, which is an approach based on a sol-gel process, enables charge redistribution across the catalyst. This allows the oxidation cycle of Fe, Co and Ni sites to be optimized, under OER operation, towards a more energetically favoured rate-limiting process. In situ and ex situ X-ray absorption spectroscopies suggest that $Fe^{2+}$ facilitates the cycling of Ni and Co species between 2+ and 3+ oxidation states. The NiFeMo was used in the industrial electrolyser system and exhibited ~17 times higher mass activity than commercial Raney Ni catalysts.

## Methods

**Density functional simulations.** We used the VASP package to perform simulations with the revised Perdew–Burke–Ernzerhof exchange correlation functional augmented with Hubbard Coulomb interaction potential (U) corrections for *d*-electrons taken from Materials project (https://materialsproject.org) ($U$(Fe) = 5.3 eV, $U$(Mo) = 4.38 eV, $U$(W) = 6.2 eV, $U$(Co) = 3.32 eV, $U$(Ta) = 2.3 eV, $U$(Re) = 2.7 eV, $U$(Nb) = 1.3 eV). Valence electrons were described with a 400-eV plane-wave basis set and 0.05-eV Gaussian smearing of electronic density. Core electrons were described using the projector augmented-wave (PAW) method. We calculated 50 different spin states for each configuration and the discussion is based on the states that yield the lowest electronic energies. The employed slabs for FeCoX systems were constructed based on a six-layer supercell of CoOOH with lateral dimensions of $5.77 \times 9.31$ Å$^2$. The reciprocal space was simulated using a $3 \times 3$ *k*-point mesh. The employed slabs for NiFeX systems were constructed based on a six-layer supercell of NiFeOOH with lateral dimensions of $6.147 \times 12.459$ Å$^2$. The reciprocal space was simulated using a $4 \times 2$ *k*-point mesh. The thermodynamic corrections to electronic energies were taken from the literature[16]. The optimized models can be found in Supplementary Data 1.

**Pourbaix diagram calculations.** Using the constructed model, we provided a systematic Pourbaix diagram calculation including over 3,000 structural optimizations. We demonstrated surface coverage and the terminal groups for both FeCo and NiFe oxyhydroxides. For each type of oxyhydroxide, we counted the possible surface terminal groups, including the empty site, O-terminated and OH-terminated groups. For each configuration, we used ISPIN = 2 in the VASP package to relax the magnetization. We then tested 50 different spin states near the relaxed magnetization using NUPDOWN in the VASP package and chose the configuration with the lowest energy. For instance, if the ISPIN = 2 calculation gave magnetization = 70, we re-made the optimization using all the 51 possibilities NUPDOWN ∈ [45, 95]. In total, the Pourbaix diagram was obtained through 6,630 calculations. The applied voltage corrections and pH corrections were performed using the following equation:

$$\Delta G_{\mathrm{corr}} = \Delta G - eU - 0.059\mathrm{pH} \quad (1)$$

where $U$ is the applied voltage and $e$ is the electron transferred during the electrochemical reaction. The pH variation can be evaluated using the following chemical equation:

$$* + H_2O \rightarrow O^* + 2H^+ + 2e^- \quad (2)$$

$$* + H_2O \rightarrow OH^* + H^+ + e^- \quad (3)$$

The Pourbaix diagram calculation was made to obtain the surface coverage and the terminal groups for both FeCoX oxyhydroxides and NiFeX oxyhydroxides. The related results are provided as Supplementary Figs. 2 and 6 for the FeCo and NiFe systems, respectively.

**Chemicals.** Iron (III) chloride ($FeCl_3$), cobalt (II) chloride ($CoCl_2$), nickel chloride ($NiCl_2{\cdot}6H_2O$), tungsten (VI) chloride ($WCl_6$), molybdenum (V) chloride ($MoCl_5$), Niobium chloride ($NbCl_5$), Tantalum chloride ($TaCl_5$), Rhenium chloride ($ReCl_5$), ethanol (≥99.5%) and propylene oxide (≥99%) were purchased from Sigma-Aldrich. $^{57}Fe_2O_3$ for preparing $^{57}FeCl_3$ was bought from Cyclotron Instruments. All the chemicals were used without further purification.

**Synthesis of multimetal oxyhydroxides.** All multimetal oxyhydroxides were synthesized using a modified aqueous sol-gel technique[16]. For every ternary mutltimetal oxyhydroxide, the molar ratio of its three metal chloride precursors was 1:1:1. Taking NiFeMo, for example, $NiCl_2{\cdot}6H_2O$ (0.9 mmol), anhydrous $FeCl_3$ (0.9 mmol) and $MoCl_5$ (0.9 mmol) were first dissolved in ethanol (4 ml) in a vial. Then a trace amount of deionized water (0.21 ml) with ethanol (2 ml) was prepared in another vial. After chilling, the solutions were mixed and propylene oxide (1 ml) was slowly added to the mixed solution. Thereafter, a wet gel was formed. The wet gel was aged for 24 h and soaked in acetone for another 5 days. Then the wet gel was dried in a vacuum or with supercritical $CO_2$ at room temperature. For the FeCoMoW or NiFeMoW samples, anhydrous $FeCl_3$ (0.7 mmol), $CoCl_2$ or $NiCl_2{\cdot}6H_2O$ (0.7 mmol), $MoCl_5$ (0.7 mmol) and $WCl_6$ (0.7 mmol) were dissolved in ethanol (4 ml) in a vial. The remainder of the procedure was the same. FeCo, NiFe and other ternary oxyhydroxides were synthesized following a process similar to that for NiFeMo oxyhydroxides.

**Synthesis of multimetal oxyhydroxides containing $^{57}$Fe.** $^{57}FeCl_3$ was firstly prepared by dissolving $^{57}Fe_2O_3$ in excess concentrated hydrochloric acid solution. Then the clear orange solution was evaporated via vacuum distillation until the slurry was formed, which was dissolved in ethanol. The remaining steps were the same as above.

**Characterization.** High-resolution transmission electron microscopy, selected-area electron diffraction and energy-dispersive X-ray spectroscopy were carried out using a Hitachi HF3300 electron microscope at an accelerating voltage of 200 kV. The samples were prepared by dropping catalyst powder dispersed in ethanol onto carbon-coated copper TEM grids (Ted Pella) using micropipettes, which were then dried under ambient conditions. The powder XRD patterns were measured on a Bruker D8 Advance spectrometer.

**XAS measurements.** Ex situ sXAS measurements were performed at the Spherical Grating Monochromator (SGM) beamline of the Canadian Light Source, the BL08U1-A beamlines at Shanghai Synchrotron Radiation Facility and the 4B9B beamline of Beijing Synchrotron Radiation Facility. All samples were scanned from 700 to 735 eV in 0.1 eV steps for the Fe $L_2$ and $L_3$ absorption edges and from 765 to 820 eV in 0.1 eV steps for the Co $L_2$ and $L_3$ absorption edges. Surface-sensitive absorption spectra were recorded using TEY.

In situ sXAS measurements were performed at the SGM beamline of the Canadian Light Source. The window of the sample cells was mounted at an angle of roughly 45° with respect to both the incident beam and the detectors. All measurements were made at room temperature in the fluorescence mode using Amptek silicon drift detectors (SDDs) with 1,024 emission channels (energy resolution ~120 eV). Four SDDs were employed simultaneously. For every edge, the scanning time was 30 s and the scans were repeated ten times, and the fluorescence of every edge was collected at the same absorption edge. The partial fluorescence yield was extracted from all SDDs by the summation of the corresponding metal L emission lines.

In situ and ex situ hard XAS measurements were performed at the 1W1B beamline of the Beijing Synchrotron Radiation Facility, the BL14W1 beamline at the Shanghai Synchrotron Radiation Facility, the SuperXAS beamline at the Swiss Light Source and the Taiwan Photon Source 44A beamline. The in situ experiment was conducted in a homemade triangular electrochemical cell, and working electrodes were prepared by loading catalyst samples on carbon paper. The spectra were obtained from 8.1 to 9.1 keV for Ni K-edge XAS, 6.8 to 7.7 keV for Fe K-edge XAS, 7.5 to 8.6 keV for Co K-edge XAS, 19.8 to 20.8 keV for Mo K-edge XAS, 10.0 to 11.0 keV for W $L_3$-edge XAS and at 0.5 eV steps at the near edge.

**Mössbauer spectroscopy measurements.** The Mössbauer experiments were carried out using an off-line Mössbauer spectrometer in APS Mössbauer Laboratory (Advanced Photon Sources, Argonne National Laboratory) using a $^{57}$Co source, and not a synchrotron radiation source. The $^{57}$Co source at the APS Mössbauer Laboratory was 10 mCi and it was newly purchased. Data analysis was conducted using in-house software.

**Electrochemical measurements.** Electrochemical measurements were performed using a three-electrode configuration connected to Autolab PGSTAT302N and PGSTAT204N. The working electrode was carbon paper (TGP-H-060, TORAY) or Ni foam (thickness, 1.8 mm). Hg/HgO and platinum plates were used as reference and counter electrodes, respectively. To load the catalyst on the working electrode, 10 mg of catalyst was dispersed in 1 ml of ethanol, followed by the addition of 80 µl of Nafion solution. The suspension was sonicated for 30 min to prepare a homogeneous ink. The catalytic electrode was prepared by spray coating the catalyst ink on carbon paper or Ni foam with a loading mass of about 1.67 mg cm$^{-2}$. The area of the catalytic electrode was fixed to $0.5 \times 0.5$ cm$^2$ by coating with

polyimide tape or water-resistant silicone glue for electrochemical testing. Cyclic voltammetry measurements at 50 mV $s^{-1}$ were performed for three cycles before the recording of linear scan voltammetry at 5 mV $s^{-1}$ for each sample.

The performances tested under industrial conditions (Supplementary Figs. 26–29) were done on Ni foam at 30% KOH solution with a temperature of 85 ± 1 °C. The industrial-scale measurements were performed using an electrolyser at the Purification Equipment Research Institute of CSIC, China (http://www.peric718.com/Home/). A 10 × 10.5 $cm^2$ NiFeMo electrode and commercial Ru electrode were used as anode and cathode, respectively. A commercial Raney Ni electrode was used as a control.

We used electrochemical impedance spectroscopy to determine the uncompensated resistance ($R$). The resistance values were 2.3 Ω for NiFe, 2.4 Ω for NiFeMo, 2.4 Ω for NiFeW, 2.1 Ω for NiFeTa, 2.6 Ω for NiFeNb, 2.8 Ω for NiFeRe, 2.4 Ω for NiFeMoW, 2.5 Ω for FeCo, 2.7 Ω for FeCoW, 2.3 Ω for FeCoMo, 2.2 Ω for FeCoTa, 2.4 Ω for FeCoNb, 2.6 Ω for FeCoRe and 2.1 Ω for FeCoMoW on carbon paper electrode. The resistance values were 0.37 Ω for NiFe, 0.38 Ω for NiFeMo, 0.37 Ω for NiFeW, 0.35 Ω for NiFeTa, 0.34 Ω for NiFeNb, 0.36 Ω for NiFeRe, 0.35 Ω for NiFeMoW, 0.39 Ω for FeCo, 0.37 Ω for FeCoW, 0.36 Ω for FeCoMo, 0.35 Ω for FeCoTa, 0.36 Ω for FeCoNb, 0.35 Ω for FeCoRe and 0.36 Ω for FeCoMoW on Ni foam electrode. At all potentials tested on carbon paper and Ni foam electrodes, the potential was manually corrected using Ohm's law:

$$E = E_{\text{applied}} - 95\%\, iR \tag{4}$$

where $E_{\text{applied}}$ is applied potential, $i$ is the current measured and there is compensation for 95% of the resistance $R$.

**TOF calculations.** TOF is defined as the frequency of the reaction per active site, which is used to compare the intrinsic activity of different catalysts. For OER, the TOF value is usually calculated by the equation:

$$\text{TOF} = \frac{\text{j} \times \text{A} \times \eta}{4 \times \text{F} \times \text{n}} \tag{5}$$

where $j$ is the current density after 95% $iR$ compensation, $A$ is the geometric area of the electrode, $\eta$ is the Faradic efficiency, $F$ is Faraday's constant and $n$ is the molar number of active sites. In our study, we assumed Ni and Co as active sites for NiFeX and FeCoX catalysts, and the number $n$ was estimated via the total loading mass, according to the equation:

$$n = \frac{m \times N_{\text{A}}}{M_{\text{w}}} \tag{6}$$

where $m$ is the loading mass, $N_A$ is Avogadro's constant and $M_w$ is the molecular weight of the catalysts.

## Data availability

The data that support the findings of this study are available on the Zenodo platform (https://zenodo.org/record/4008830) (ref. [31]).

Received: 16 February 2019; Accepted: 15 September 2020;
Published online: 19 October 2020

## References

1. Zhang, J., Zhao, Z., Xia, Z. & Dai, L. A metal-free bifunctional electrocatalyst for oxygen reduction and oxygen evolution reactions. *Nat. Nano.* **10**, 444–452 (2015).
2. Ng, J. W. D. et al. Gold-supported cerium-doped NiOx catalysts for water oxidation. *Nat. Energy* **1**, 16053 (2016).
3. Liang, Y. et al. $Co_3O_4$ nanocrystals on graphene as a synergistic catalyst for oxygen reduction reaction. *Nat. Mater.* **10**, 780–786 (2011).
4. Seh, Z. W. et al. Combining theory and experiment in electrocatalysis: Insights into materials design. *Science* **355**, eaad4998 (2017).
5. Seitz, L. C. et al. A highly active and stable $IrO_x/SrIrO_3$ catalyst for the oxygen evolution reaction. *Science* **353**, 1011–1014 (2016).
6. Bergmann, A. et al. Unified structural motifs of the catalytically active state of Co(oxyhydr)oxides during the electrochemical oxygen evolution reaction. *Nat. Catal.* **1**, 711–719 (2018).
7. Guan, J. et al. Water oxidation on a mononuclear manganese heterogeneous catalyst. *Nat. Catal.* **1**, 870–877 (2018).
8. Martin-Sabi, M. et al. Redox tuning the Weakley-type polyoxometalate archetype for the oxygen evolution reaction. *Nat. Catal.* **1**, 208–213 (2018).
9. Roy, C. et al. Impact of nanoparticle size and lattice oxygen on water oxidation on $NiFeO_xH_y$. *Nat. Catal.* **1**, 820–829 (2018).
10. Jouny, M., Luc, W. & Jiao, F. High-rate electroreduction of carbon monoxide to multi-carbon products. *Nat. Catal.* **1**, 748–755 (2018).
11. Jouny, M., Luc, W. & Jiao, F. General Techno-Economic analysis of $CO_2$ electrolysis systems. *Ind. Eng. Chem. Res.* **57**, 2165–2177 (2018).
12. Galán-Mascarós, J. R. Water oxidation at electrodes modified with earth-abundant transition-metal catalysts. *ChemElectroChem* **2**, 37–50 (2015).
13. Subbaraman, R. et al. Trends in activity for the water electrolyser reactions on 3*d* M(Ni,Co,Fe,Mn) hydr(oxy)oxide catalysts. *Nat. Mater.* **11**, 550–557 (2012).
14. Roger, I., Shipman, M. A. & Symes, M. D. Earth-abundant catalysts for electrochemical and photoelectrochemical water splitting. *Nat. Rev. Chem.* **1**, 0003 (2017).
15. Fabbri, E. et al. Dynamic surface self-reconstruction is the key of highly active perovskite nano-electrocatalysts for water splitting. *Nat. Mater.* **16**, 925–931 (2017).
16. Zhang, B. et al. Homogeneously dispersed multimetal oxygen-evolving catalysts. *Science* **352**, 333–337 (2016).
17. Rosalbino, F., Delsante, S., Borzone, G. & Scavino, G. Electrocatalytic activity of crystalline Ni–Co–M (M = Cr, Mn, Cu) alloys on the oxygen evolution reaction in an alkaline environment. *Int. J. Hydrog. Energy* **38**, 10170–10177 (2013).
18. Chen, J. Y. C., Miller, J. T., Gerken, J. B. & Stahl, S. S. Inverse spinel $NiFeAlO_4$ as a highly active oxygen evolution electrocatalyst: promotion of activity by a redox-inert metal ion. *Energy Environ. Sci.* **7**, 1382–1386 (2014).
19. Gerken, J. B., Shaner, S. E., Masse, R. C., Porubsky, N. J. & Stahl, S. S. A survey of diverse earth abundant oxygen evolution electrocatalysts showing enhanced activity from Ni-Fe oxides containing a third metal. *Energy Environ. Sci.* **7**, 2376–2382 (2014).
20. Friebel, D. et al. Identification of highly active Fe sites in (Ni,Fe)OOH for electrocatalytic water splitting. *J. Am. Chem. Soc.* **137**, 1305–1313 (2015).
21. Bajdich, M., García-Mota, M., Vojvodic, A., Nørskov, J. K. & Bell, A. T. Theoretical investigation of the activity of cobalt oxides for the electrochemical oxidation of water. *J. Am. Chem. Soc.* **135**, 13521–13530 (2013).
22. Novák, M. et al. Primary oxide minerals in the system $WO_3$–$Nb_2O5$–$TiO_2$–$Fe_2O_3$–FeO and their breakdown products from the pegmatite No. 3 at Dolní Bory-Hatě, Czech Republic. *Eur. J. Mineral.* **20**, 487–499 (2008).
23. Kuepper, K. et al. Electronic and magnetic properties of highly ordered $Sr_2FeMoO_6$. *Phys. Stat. Sol. (a)* **201**, 3252–3256 (2004).
24. Liu, X., Yang, W. & Liu, Z. Recent progress on synchrotron-based in-situ soft X-ray spectroscopy for energy materials. *Adv. Mater.* **26**, 7710–7729 (2014).
25. de Groot, F. M. F. et al. 1*s*2*p* resonant inelastic X-ray scattering of iron oxides. *J. Phys. Chem. B* **109**, 20751–20762 (2005).
26. Mitsui, T. in *Magmas Under Pressure* (eds Kono, Y. & Sanloup, C.) 179–210 (Elsevier, 2018).
27. Zheng, X. et al. Theory-driven design of high-valence metal sites for water oxidation confirmed using in situ soft X-ray absorption. *Nat. Chem.* **10**, 149–154 (2018).
28. Liu, P. F., Yang, S., Zheng, L. R., Zhang, B. & Yang, H. G. Mo6+ activated multimetal oxygen-evolving catalysts. *Chem. Sci.* **8**, 3484–3488 (2017).
29. Liu, P. F., Yang, S., Zheng, L. R., Zhang, B. & Yang, H. G. Electrochemical etching of α-cobalt hydroxide for improvement of oxygen evolution reaction. *J. Mater. Chem. A* **4**, 9578–9584 (2016).
30. Qiu, Z., Tai, C.-W., Niklasson, G. A. & Edvinsson, T. Direct observation of active catalyst surface phases and the effect of dynamic self-optimization in NiFe-layered double hydroxides for alkaline water splitting. *Energy Environ. Sci.* **12**, 572–581 (2019).
31. Zhang, B. et al. High-valence metals improve OER performance by modulating 3*d* metal oxidation cycle energetics. *Zenodo Digital Repository* https://doi.org/10.5281/zenodo.4008830 (2020).

## Acknowledgements

This work was supported by MOST (grant no. 2016YFA0203302), NSFC (grant nos. 21875042, 21634003 and 51573027), STCSM (grant nos. 16JC1400702 and 18QA1400800), SHMEC (grant no. 2017-01-07-00-07-E00062) and Yanchang Petroleum Group. This work was also supported by The Programme for Professor of Eastern Scholar at Shanghai Institutions of Higher Learning. This work was supported by the Ontario Research Fund—Research Excellence Program, NSERC and the CIFAR Bio-Inspired Solar Energy program. This work has also benefited from the use of the SGM beamlines at Canadian Light Source; the 1W1B and 4B9B beamlines at the Beijing Synchrotron Radiation Facility; the BL14W1, BL08U1-A beamline at Shanghai Synchrotron Radiation Facility; and the 44A beamline at Taiwan Photon Source (TPS). Mössbauer spectroscopy measurements were conducted at the Advanced Photon Source, a Department of Energy (DOE) Office of Science User Facility operated for the DOE Office of Science by Argonne National Laboratory under Contract DE-AC02-06CH11357. We acknowledge the Paul Scherrer Institut, Villigen, Switzerland, for provision of synchrotron radiation beamtime at the beamline SuperXAS of the SLS and would like to thank M. Nachtegaal for assistance. We thank M. García-Melchor and Y. Zhang for discussions on DFT calculations. We thank J. Wu for the assistance with the TEM measurements. We thank R. Wolowiec and D. Kopilovic for their assistance. For computer time, this research used the resources of the Supercomputing Laboratory at KAUST.

## Author contributions

E.H.S., H.P., B.Z. and L.C. supervised the project. B.Z. designed the project. L.W. and B.Z. carried out the experiments. Z.C., S.M.K. and Z.W. carried out the DFT simulations. L.W., X.Z., L. Zhang, Y.W., C.W.P., L. Zheng and J.L. carried out XAS measurements.

T.R. assisted in situ XAS experiments. L.W., F.P.G.A., R.C. and J.L. performed the XAS results analysis. O.V., Z.W. and P.D.L. assisted with the DFT simulations. W.B. and E.E.A. carried out the Mössbauer spectroscopy experiment and data analysis. C.T.D. and Y.H. contributed to discussions about the experiments. Y.J. and Y.L. contributed to the discussions about DFT simulations. Y.Z. assisted with TEM and XRD measurements. B.Z., L.W., Z.C., F.P.G.A., S.M.K., H.P. and E.H.S. wrote the manuscript. All authors discussed the results and assisted during manuscript preparation.

## Competing interests

The authors declare no competing interests.

## Additional information

**Supplementary information** is available for this paper at https://doi.org/10.1038/s41929-020-00525-6.

**Correspondence and requests for materials** should be addressed to B.Z., L.C., H.P. or E.H.S.

**Reprints and permissions information** is available at www.nature.com/reprints.

**Publisher's note** Springer Nature remains neutral with regard to jurisdictional claims in published maps and institutional affiliations.